Through-barrier sub-mm electromagnetic induction imaging with atomic magnetometers

Han Yao (姚涵), Ningzhen Yin (尹宁真), Raymond Lee, Gehang Liu (刘歌行), and Ferruccio Renzoni

Abstract-Eddy-current non-destructive testing is widely used for the detection of cracks and fatigue in metallic structures. This is usually done by sweeping an inductor coil over the sample of interest, while monitoring changes in the coil response. While this may allow for the detection of sub-mm cracks and defects, the technique lacks of penetrating power through barriers. This work addresses such a capability gaps. We demonstrate a mechanically translatable system based on an atomic magnetometer that allows for sub-mm resolution while simultaneously allowing also for penetration through shields. The adoption of a radio-frequency atomic magnetometer as a sensor allows for the operation of the system at low frequency, with high sensitivity achieved by introducing several technical solutions which lead to enhanced performances, with respect to existing systems, and improved stability of the instrument while scanning over the target object. The obtained enhanced performances are highlighted by the demonstrated ability to detect and image gaps as small as 0.27 mm concealed behind a shield consisting of a 1.50 mm rubber sheet and a 0.42 mm aluminium sheet.

Index Terms—sub-mm electromagnetic induction imaging, atomic magnetometers.

I. INTRODUCTION

E LECTROMAGNETIC induction imaging (EMI) [1] is a non-contact non-destructive imaging technique. It operates by generating eddy currents in a target sample using an oscillating low-frequency primary magnetic field. These eddy currents subsequently produce a secondary magnetic field. The measurement of the secondary field allows for the electromagnetic properties of the target to be determined, including the conductivity (σ) , the permittivity (ε) and the magnetic permeability (μ) . The implementation of position-resolved measurements enables the generation of an image that maps these properties in space.

In the past decades, EMI has been widely used in a broad range of industries for the assessment of the integrity of metallic structures [2]–[6]. EMI is appealing as it is contactless, low-cost and does not involve harmful ionizing radiation. However, in the standard approach to EMI, an inductive coil is used as a sensor. This prevents the operation at low frequency, a regime where inductors lose sensitivity [7]. Thus the technique has been lacking of penetrating power through shields, as this would require operation at low frequency, so to obtain

Corresponding author: Ferruccio Renzoni (email: f.renzoni@ucl.ac.uk). Han Yao is with the School of Physics, Nanjing University of Science and Technology, Nanjing 210094, China. Ningzhen Yin, Raymond Lee, Gehang Liu, and Ferruccio Renzoni are with the Department of Physics and Astronomy, University College London, Gower Street, London WC1E 6BT, UK.

a skin depth larger than the shield thickness. This limited the analysis of the integrity of structures to superficial cracks and defects. The use of atomic magnetometers (AMs) [8] in EMImodality as sensors [9], [10] overcomes such a limitation, as the fundamental sensitivity limit of atomic magnetometers is frequency-independent [7]. Thus the use of atomic magnetometers allows one to operate the EMI system with high sensitivity at low frequency, and penetrate through barriers [11]. The new opportunities offered by EMI-AM sparked a lot of attention and further development of the technology were reported by several groups [12]–[17]. However, most of the reported proof-of-concepts of through-barrier imaging were based on a static sensor [14], with the sample of interest mechanically translated over the sensor, a configuration not suited for real-world application. The required capability to detect cracks through barrier by sweeping an atomic sensor over the structure of interest was still beyond existing systems, with the only translatable atomic sensor demonstrated to date [18] still lacking in the required performances. Slow progress in the development of a translatable atomic sensor suitable for highsensitivity operation in magnetically unshielded environment is due to the difficult task of satisfying conflicting requirements: to operate with extreme sensitivity and to cope with a continuously changing magnetic environment, as encountered while translating the atomic sensor.

In this work we present a design of translatable atomic sensor which allows for maintaining high sensitivity while scanning over the object of interest. This closes the abovementioned capability gap for EMI-AM systems and specifically it allows us to demonstrate through-barrier electromagnetic induction imaging of sub-mm gaps in metallic structures using a mechanically translatable unshielded atomic magnetometer. This mimicks the detection of cracks in metallic structures behind shields, a common situation in industry where supporting structures may be concealed behind metal sheets. The demonstrated experimental arrangement satisfies many requirements of real-world scenarios, including the ability to operate in unshielded environment and the ability to sweep the sensor over the surface of the structure.

The demonstrated through-barrier sub-mm imaging was made possible by several technical innovations, that significantly improved the performances of previously demonstrated EMI-AM systems. These innovations and the resulting achieved capabilities are reported in this work. This paper is organised as follows. Section II introduces the instrument, describing in detail the features that lead to improved performances with respect to existing systems. Section III presents results of imaging of gaps in metallic structures. Several target

objects are considered, with barriers of different thickness and material introduced. In section IV conclusions are drawn.

II. EXPERIMENTAL SETUP

The EMI-AM apparatus used in this work is based on a previously demonstrated mechanically-translatable system [18], with the introduction of specific innovations, developed in the context of the present work, enabling increased penetration and resolution.

The EMI apparatus has been thoroughly described in previous publications [18], [19], therefore, here we only summarise essential details, to then cover the three innovations used to enhance imaging penetration and spatial resolution.

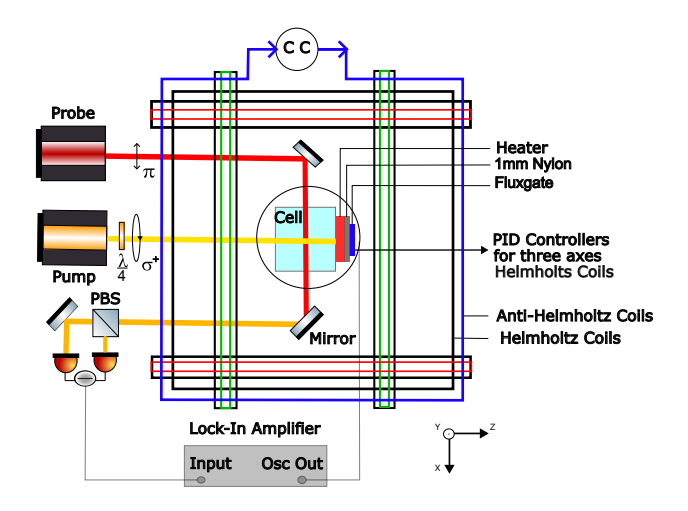


Fig. 1. Schematic overview of the sensor head. The probe and pump light is generated by vertical-cavity surface-emitting lasers. CC: constant current which flows through all three axes of anti-Helmholtz coils; $\lambda/4$: quarter-wave plate; PBS: polarised beam splitter. The black square and black rectangles surrounding the cell represent the Helmholtz coils along the three different axes. The blue, green and red rectangles show the three pairs of anti-Helmholtz coils installed on top of the original frame of the Helmholtz coils for the x-, y- and z-axis. To this purpose 9 more turns are wound on top the x-axis Helmholtz coils and 5 more turns are installed along both y- and z-axis. The heater is installed next to the cell, with a distance of 12.3 mm between the centre of the cell and the fluxgate.

The sensor head consists of a mechanically translatable radio-frequency atomic-magnetometer (RF-AM) weighing 1.49 kg and measuring $110.0 \times 110.0 \times 145.0~\mathrm{mm}^3~(W \times L \times H)$. It houses all optical and electronic components which are secured by a nylon support fabricated through selective laser sintering (SLS). As shown in Fig.1, the unit includes vertical-cavity surface-emitting lasers (VCSELs), magnetic field compensation coils, and a vapour cell, all integrated within the sensor head without requiring external optical inputs or outputs. Additionally, it features a polarimeter to monitor the probe light polarization rotation, and an RF coil, essential for driving the atomic precession and inducing eddy currents in the target sample.

At the core of the sensor head is a cubic glass cell with dimensions $(20.0\times 20.0\times 20.0\, mm^3)$ which contains isotopically enhanced ^{87}Rb vapour and $20\, Torr$ of N_2 buffer gas. The magnetic bias field (B_{bias}) for tuning the magnetometer is generated and stabilized by three pairs of orthogonal

Helmholtz coils (35 turns each coil, 0.20 mm diameter copper wire) surrounding the sensor. The RF coil (SBCP-80HY681H KEMET), positioned above the cell along the y-axis, has an inductance of 680 μH and a core size of 8.0×10.0 mm. It is driven at the frequency ω_{RF} , which is swept across the Larmor frequency ω_0 determined by B_{bias} along the z-axis.

A three-axis fluxgate magnetic sensor (Bartington MAG612) which is 12.3 mm deviated from the cell provides feedback to three servo controllers, which actively adjust the currents in the three Helmholtz coils to provide stable bias field in the noisy environment. The electrical unit of the system includes two current controllers, two temperature controllers for the VCSEL lasers, power supplies, proportional-integral-derivative (PID) controllers for the three-axis coils, and a lock-in-amplifier (LIA) that powers the RF coil and processes the polarimeter signal.

The sensor head is mounted on a motorised 2D mechanical translation stage. In this way the sensor can be swept over the target object. An image of a target object is generated by acquiring magnetic resonances at different positions, with each position defining a pixel. For each pixel, the RF coil frequency is swept around ω_0 to obtain a magnetic resonance response. The in-phase (X) and out-of-phase (Y) components, with respect to the excitation signal, are acquired via the LIA and fitted as Lorentzian line shapes. These processes facilitate the extraction of key parameters: amplitude, resonant frequency and linewidth of the magnetic resonance signal. Near resonant imaging [20] is utilized to produce more stable images with improved contrast. The procedure involves using the fitted resonance parameters to continuously monitor the resonant frequency at each pixel. The in-phase and out-ofphase components at a desired detuning from resonance, are extracted from the fitting results of each pixel. Then, the radius $R = \sqrt{X^2 + Y^2}$ and phase $\Phi = \arctan(Y/X)$ at this detuning are calculated for imaging purposes as well.

As part of the present work, a significant improvement in penetrating power through shields and resolution is achieved by introducing three innovations relative to existing mechanically translatable systems. First, while in previous work [18], [19] a naturally occurring isotopic mixture of Rb at room temperature was found to be sufficient for imaging, in the instrument demonstrated here the installation of a heater to raise the temperature of the vapour cell significantly improves the imaging performance via an increase in signal strength, hence sensitivity. Second, beyond the original Helmholtz coils, the addition of three pairs of orthogonal anti-Helmholtz coils has been implemented to compensate for ambient gradients, and further improve the quality of the magnetometer response. Lastly, the introduction of a low-pass filter into the ambient field stabilisation loop allows for the operation of the system at low frequency without interference between different axes. These three technical developments are described in detail in the following, together with the associated benefits.

A. Heater

A heater is installed between the fluxgate and the Rb cell. The heater is made of 70 turns of copper wire wound on a nylon piece of 1.30 mm thickness. The diameter of the copper wire is 0.30 mm and its resistance is 2.08 Ω . To suppress the magnetic field generated by the heater current, copper wires are paired to cancel the magnetic field generated by the currents of the same magnitude and opposite direction. To determine the temperature of the heater, a resistance temperature sensor (RTD) PT1000 is placed in contact with the wires and read out via a DAQ chassis (Model cDAQ 9171, National Instrument) while another DAQ (Model USB6001, National Instrument) regulates the square-wave amplified current flowing through the heating wire.

A standard optimisation procedure [21] was adopted to identify the cell temperature which leads to the best sensitivity. The heater temperature was optimised to 87°C for the lowest ratio of the atomic magnetic resonance linewidth over amplitude. When compared to room temperature operation, the magnetometer's linewidth increased by 43%, the ratio decreased by 70%, and the signal intensity rose by 140%. These enhancements prove the significant role of increased rubidium vapour temperature in improving the magnetometer's performance, which is crucial for gaining higher resolution in imaging results.

B. Anti-Helmholtz Coils

Further improvement in performances is achieved by compensating for the ambient magnetic field gradients. To this purpose, three pairs of orthogonal anti-Helmholtz coils with side lengths of 10.0 cm have been wound on top of the existing Helmholtz coils. The spacing between each pair of these coils is 44.0 mm. An additional 9 turns of anti-Helmholtz copper coils have been added along the x-axis and 5 additional turns along both the y- and z-axis. The same type of copper wire adopted for the Helmholtz coils is used for the anti-Helmholtz coils. The current through each coil direction has been optimised to minimise the atomic resonance linewidth. Fig. 2 details the procedure and the results obtained for the optimisation along the x-axis: the atomic resonance linewidth was measured for different values of the current circulating in the x-axis anti-Helmholtz coil pair. The linewidth displays a strong dependence on this current, and a minimum is readily identified. The current corresponding to such a minimum was selected as a result of the procedure. The same approach was followed to optimise the current in the y- and z-axis anti-Helmholtz coil pairs. As shown in Fig. 3, the installation of the three-axis anti-Helmholtz coils further narrows the linewidth and increases the signal amplitude.

C. Low-Pass Filter

Through-barrier EMI requires the operation of the radio-frequency atomic magnetometer at low frequency, a regime where we observed distorted atomic magnetic resonance line-shapes, as shown in Fig. 4. We identified the source of the problem to be the conflict between the feedback loops along the three different axes used to stabilise the ambient field. This is mostly relevant at low frequency where the frequency of operation of the atomic magnetometer falls within the bandwidth of the feedback loop. In the present work, low-pass

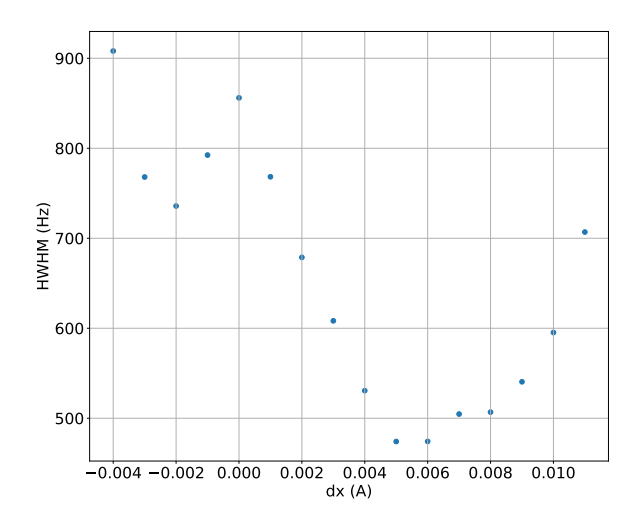


Fig. 2. Optimisation of the compensation of magnetic field gradients: the half width at half maximum (HWHM) of the magnetic resonance is plotted as a function of the current circulating in the anti-Helmholtz coil pair along the x-axis. The current leading to the minimum linewidth is selected as the optimum value for the x-axis gradient compensation.

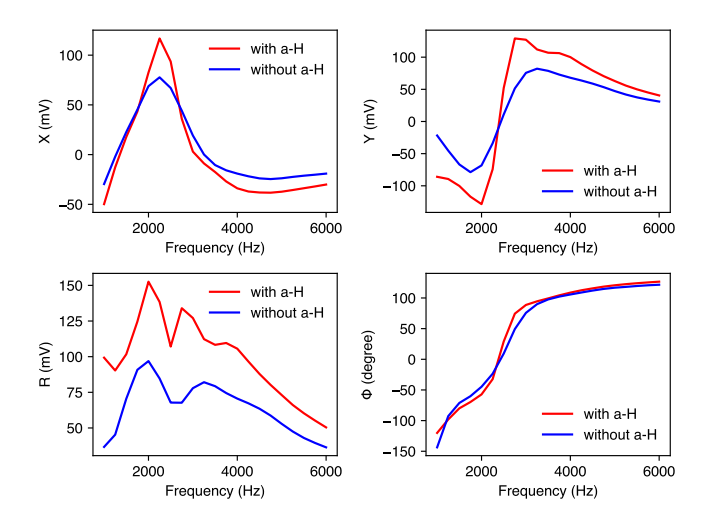


Fig. 3. Improvement in performance of the RF-AM as a result of the installation of anti-Helmholtz (a-H) coils, as quantified by observing the atomic magnetic resonance. The red lines refer to the X, Y, R and Φ components of the demodulation signal as a function of the sweeping RF frequency, with the background gradient field compensated via anti-Helmholtz coils. The blue lines refer to the resonance taken without any compensation of the gradient field. In X, Y and R components of LIA, signal intensity is significantly enhanced. In the X component, one can observe a narrower linewidth and accordingly a sharper change near resonance in Y and Φ components.

filters (LPFs) were introduced within the feedback loops to reduce the loop bandwidths and therefore suppress any conflict with the operation of the magnetometer. Table I reports the best configuration of LPF identified, with a single Butterworth LPF (Stanford Research Systems SIM965 Analog Filter) introduced in the feedback loop controlling the compensation along the y-axis, with a cut-off frequency of 200 Hz and 24 dB/octave roll-off in the stopband.

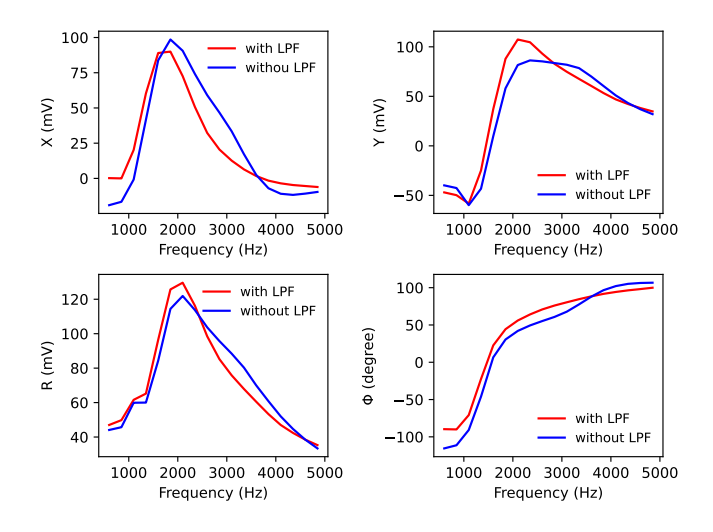


Fig. 4. Effect of the application of a low-pass filter (LPF) with results for the configuration without low-pass filter reported for comparison. The RF-AM is tuned to the resonance frequency of 2.0 kHz. As from the X and R images, the use of a LPF results in a reduction by 28% of the linewidth of the magnetic resonance. Moreover, the shape of the resonance curve becomes smoother and closer to a standard Lorentzian curve. In the same way, the Y response exhibits a sharper change when the LPF is applied, and a lineshape better approximating a dispersive lineshape.

TABLE I OPTIMISED LPF CONFIGURATION IN COMPARISON WITH THE CONFIGURATION WITHOUT LPF. THE RESONANCE FREQUENCY AND LINEWIDTH ARE EXTRACTED VIA A FIT OF THE X COMPONENT OF THE MAGNETIC RESONANCE, FOR WHICH THE ADJUSTED \mathbb{R}^2 IS ALSO REPORTED.

Y/X/Z Axis LPF Cutoff Frequency (Hz)	Frequency (Hz)	Linewidth (Hz)	Ratio (Hz/mV)	Adj R ²	Signal Intensity (mV)
0/0/0	2102.8	801.5	8.2	0.87	98.34
200/0/0	1835.6	577.2	6.0	0.95	95.50

III. IMAGING RESULTS

This Section presents results of imaging with the described sensor, and quantifies the perfomances of the instrument by considering different combinations of targets and barriers.

The imaging procedure adopted for all presented results is as follows. Eddy currents are induced in the target when excited by an oscillating primary magnetic fields via the inductor. A 33.4 nT magnetic field B_{RF} was applied in this work. The combination of the primary and secondary fields gives rise to a change that is detected by the RF-AM. The target is placed on a plastic plate above the sensor head with a 0.1 mm standoff between the target and the top of the inductor. EMI was performed by translating the sensor head over the target sample. For each position, the RF frequency is swept around resonance with the four outputs of the lock-in amplifier X, Y, R and Φ collected during the frequency sweeping.

Different target samples were imaged to highlight the capabilities of the presented technology with respect to the two key parameters: resolution and penetration through barriers. Thus, combinations of metallic plates with different features and shields were considered. Specifically, three different aluminium target objects were imaged in this section: a plate with 1.00 mm diameter pinhole, a ring with a 0.68 mm width gap, and two plates separated by a narrow taper gap. These three target objects are imaged under the same experimental conditions except for the EMI system operating frequency. The size of the scanning area was also adapted to the size of each target.

A. Pinhole

An Aluminium alignment plate with a 1.00 mm pinhole (LMR1AP, Thorlabs) is imaged at 50.0 kHz without shield and at 2.5 kHz with shield. The diameter of the plate is 33.3 mm and the thickness of the plate is 1.3 mm. The area around the 1 mm pinhole were mapped with a step size of 0.5×0.5 mm².

1) Unshielded Pinhole: The first image acquisition was done without any shielding. A set of measurements was taken to assess the stability of the imaging system while moving across the area of interest. Magnetic resonances of X, Y, R, and Φ of LIA for all the 256 pixels in the area of interest are fitted and it is found that there is only minor fluctuation in signal intensity. A more detailed analysis is carried out by fitting the magnetic resonance of each pixel to extract the resonance frequency, linewidth, signal amplitude and adjusted R^2 . The fluctuation Δ of the resonance frequency F is defined as

$$\Delta = \frac{\sqrt{\overline{(F - \overline{F})^2}}}{\overline{F}} , \qquad (1)$$

where the overline indicates average over the data set. By fitting the magnetic resonance of X component, the fluctuation of the resonance frequency is calculated to be $\Delta_X=0.1\%$. These results demonstrate that the scanning process maintains a stable and uniform magnetic field background, a pre-requisite for high-quality imaging.

Images were then generated following the procedure described in the previous section. Images for the X, Y, R and Φ components of the LIA are reported in Fig. 5. Notably, the X, R and Φ images reveal the pinhole. Among all four components, the Φ image provides the clearest and most complete circular shape. The diameter of the pinhole measured from the Φ image is 1.2 \pm 0.5 mm. While the result is consistent with the actual size of the pinhole we notice that, in general, we expect a 'lensing effect' produced by the spreading of the field lines from the object to the sensor. This will be more evident in the presence of a shield, and resulting finite lift-off, as investigated in the following.

2) Shielded Pinhole: a rubber and an aluminum shield: Subsequent measurements were devoted to a shielded pinhole. The pinhole is concealed behind a 1.50 mm rubber shield and a 0.42 mm aluminum sheet. Imaging is performed at an operating frequency of 2.5 kHz.

Atomic resonances of R component of LIA for 400 pixels of relevant area are fitted and presented in Fig.6 (a). Furthermore, by fitting the in-phase (X) components of the magnetic resonance at every pixel, the resonance frequency, linewidth, resonance amplitude and adjusted R^2 are extracted, with results in Fig.7. The fluctuation of the frequency of the X (in-phase) component is calculated to be $\Delta_X = 1.8$ %. The

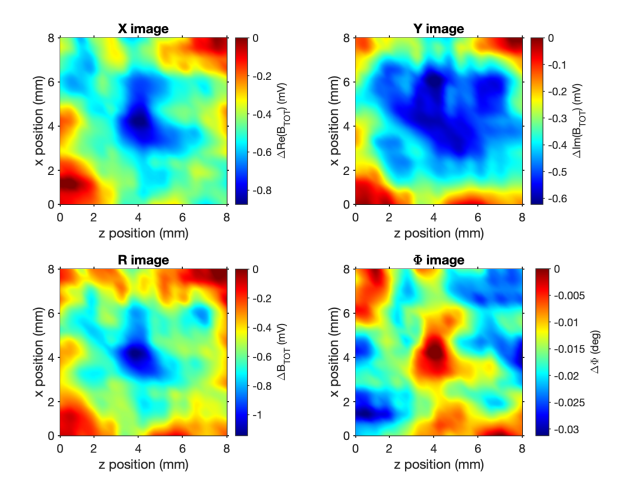


Fig. 5. Results for electromagnetic induction imaging of the unshielded 1.00 mm pinhole. The operating frequency is 50.0 kHz with the fluctuation of the resonance frequency from the X component measured to be equal to $\Delta_X=0.1\%$. Eddy currents are generated by applying a 95.00 mV signal, resulting in a current of 647.2 mA through the inductor in the RF coil. Additionally, a 33.4 nT excitation field (B_{RF}) is applied. The scan covered an area of $8.0\times8.0\,\mathrm{mm}^2$ with a pixel size of $0.5\times0.5\,\mathrm{mm}^2$. From the X, R and Φ images, a circular shape emerges that indicates that the pinhole can be observed, with the Φ image providing the best quality image. The pinhole size measured from the Φ image is $1.2\pm0.5\,\mathrm{mm}$.

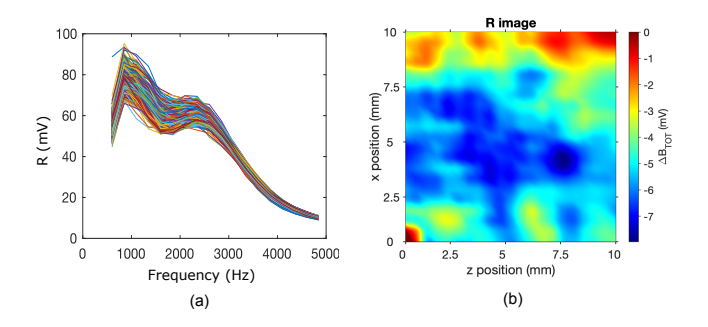


Fig. 6. Results for electromagnetic induction imaging at 2.5 kHz of the 1 mm pinhole shielded by 1.50 mm rubber and 0.42 mm aluminium sheets. The fluctuation of the frequency while scanning from the X component is $\Delta_X=1.8~\%$. (a) Magnetic resonance curves of the R component of LIA for 400 pixels constituting the imaging area. The curves overlap well with a minor change in signal amplitude. (b) The image result with the area of the scan is $(10.0\times10.0~\text{mm}^2)$ with a step size of 0.5 mm. The diameter of the pinhole is measured to be 2.1 \pm 0.5 mm.

good overlap among all curves ensures stable operation of the instrument while scanning at a low frequency such as 2.5 kHz.

An image for the R component of the shielded pinhole was generated by fitting R data and reported in Fig.6 (b). We note that the pinhole was slightly displaced in the right direction from the center of the imaging area. From the R image, the feature of the pinhole could be identified. The diameter measured from the R image is 2.1 ± 0.5 mm which is consistent with the actual size. We notice that, as the thickness of the shield is increased, the "lensing effect" is further enhanced. Thus all the measurements correspond to a size of the pinhole slightly larger than the actual size.

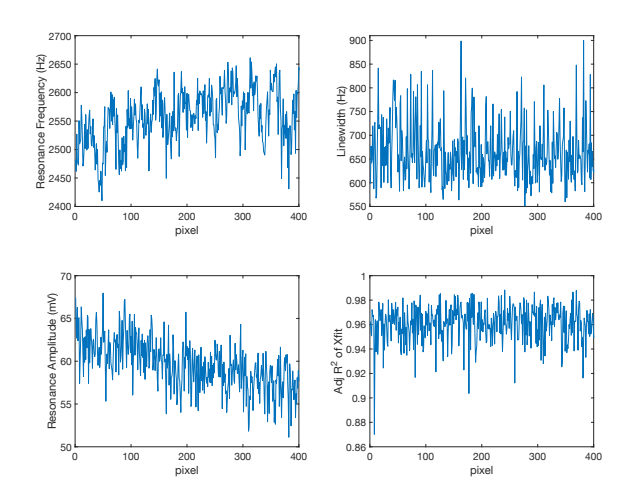


Fig. 7. The resonance frequency, linewidth, resonance amplitude and adjusted are plotted for the X (in-phase) component while scanning the shielded pinhole at an operating frequency of 2.5 kHz. The fluctuation of the resonance frequency is calculated to be $\Delta_X=1.8~\%$.

B. An aluminum ring with 0.68 mm crack

1) Unshielded Aluminium ring: We consider as target an aluminum ring which has a sub-mm crack and is shielded by a 2.82 mm thick aluminum plate. The dimensions of the ring are detailed in Fig.8. A $27.5 \times 30.0~\text{mm}^2$ image is built up with a pixel size of $0.5 \times 0.5~\text{mm}^2$.

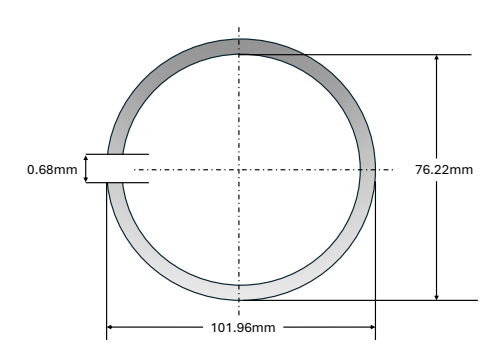


Fig. 8. Sketch of the Aluminium ring with a gap. The inner diameter of the aluminium ring is 76.22 mm and its outer diameter is 101.96 mm. The thickness of the ring is 1.15 mm. The size of the gap is 0.68 mm.

Proceeding as previously described, in Fig.9 (a), the phase Φ from the LIA for all 3300 pixels are fitted and displayed. The magnetic resonance curves for different pixels overlap consistently, with only minor fluctuations, indicating a high degree of uniformity across the measurements. By fitting the X component of the magnetic resonances, the fluctuation of the frequency for X (in-phase) is calculated to be $\Delta_X = 2.9$ %. When considered alongside the graphical data, these figures demonstrate that the stability of the instrument is not degraded by the scanning process.

Images are generated for the phase output Φ of the LIA by fitting phase magnetic resonance data, with results as in Fig.9 (b). In the amplitude-pixel plot shown in Fig.9 (a), the

 Φ component shows a sharp change in the amplitude and phase near the central resonance frequency. The phase component is less sensitive to variations in the environmental field compared to the R component. This becomes apparent by analysing the theoretical expression for the amplitude of the two responses [22]. The expression for the R component:

$$S^{(R)} = \left(S_{\text{in-phase}}^2 + S_{\text{out-of-phase}}^2\right)^{1/2}$$

$$= \frac{S_0(\gamma B_y/2) \left(1 + (\omega - \omega_0) T_2^2\right)^{1/2} T_2}{1 + (\gamma B_y/2)^2 T_1 T_2 + (\omega - \omega_0) T_2^2} , \qquad (2)$$

where T_2 is the transverse relaxation time, evidences a dependence on the amplitude B_y of the transverse magnetic field and hence a strong sensitivity to environmental fluctuations. On the other hand, the Φ response:

$$S^{(\Phi)} = \arctan\left(\frac{S_{\text{in-phase}}}{S_{\text{out-of-phase}}}\right) = \arctan\left(\frac{-1/T_2}{\omega - \omega_0}\right) .$$
 (3)

does not include a direct dependence on the magnetic field, and hence it is less sensitive to environmental fluctuations. The above reasoning justifies our choice to use the Φ component for generating the desired images.

The feature of the ring is successfully extracted from the background and shown in blue. The crack is clearly detected from the ring and shows the same colour as the background. This indicates a high contrast of the image produced. To be more quantitative, we introduce the contrast C defined as

$$C = \frac{\Phi_{max} - \Phi_{min}}{\Phi_{max} + \Phi_{min}} \ . \tag{4}$$

Results of Fig.9 (b) correspond to a contrast C = 0.45. The measured frequency from the image is 6.1 ± 0.5 mm, which is 10 times larger than the actual size of the ring. The 'lensing' effect here is very significant. This is also due to the very small size of the gap. On the one hand, matrices of data that depend on the position are normalised and then filtered by the nearest neighbour filter and thus this is an obvious consequence of applying the nearest neighbour filter. On the other hand, an important contribution to the lensing effect is due to the relatively large spread of the primary field at the object's surface. A perpendicular AC magnetic field (B_{RF}) excites spin-coherences and produces a transverse atomic polarization. According to finite-element simulations, the actual distribution of (B_{RF}) on the plane of the object is broader than the gap itself (FWHM \sim 6mm). This could be improved by using more localised driving fields or by introducing a new image processing method that takes into account the distribution of the driving field over the spatial extension of the object.

In Fig.10, the 3D contour fitting plot of the Y images of Fig.9 (b) is generated with different angles of view. In Fig. 10, (a) shows a top view of the contour fitted plot generated using the least squared fitting method, and (b) shows a cross-sectional view of the gap using the same method. In Fig.10 (a), the feature of the ring is successfully extracted from the background with a high degree of contrast. The crack in the ring can also be identified and is shown as the same colour as the background. In Fig.10 (b), the thickness of the aluminium

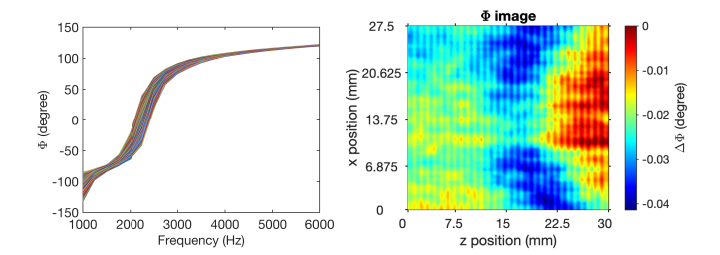


Fig. 9. Results for electromagnetic induction imaging at 2.2 kHz of the unshielded aluminium ring with a gap. While scanning, the fluctuation of the frequency is $\Delta_X=2.9$ % from the X component. (a) Plot of all 3300 pixels of the Phase (Φ) of LIA used for imaging the unshielded aluminium ring with the 0.68 mm crack. (b) The Phase (Φ) image results. The scan area is $27.5\times30.0\,\mathrm{mm^2}$ image is built up with a pixel size of $0.5\times0.5\,\mathrm{mm^2}$. The feature of the ring is successfully captured and the crack is measured to be $6.1\pm0.5\,\mathrm{mm}$.

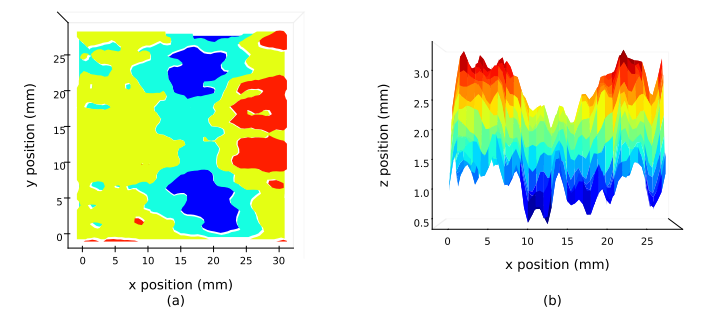


Fig. 10. Contour fitting plot of the Y images of Fig.9 with different views. (a) Top view of the contour fitted plot that uses the least-squared fitting method. It can be observed that the ring features are clearly (blue) extracted from the background (light green and cyan). The gap of the ring has been successfully detected and shown compared with the ring's blue colour in the image. (b) A cross-sectional view of the crack, a clear hollow can be observed in the image, which indicates the crack. The measured thickness of the ring is 1.5 \pm 0.5 mm.

ring can be detected and measured from the cross-sectional view of the crack. The thickness is measured as 1.5 ± 0.5 mm which is consistent with the actual thickness of the ring 1.15 mm.

2) Shielded Aluminium ring: rubber shield: Then, a scan was conducted on the same aluminium ring with a rubber shield whose thickness is 1.50 mm. In Fig. 11 (a), data for the X component from the LIA for all 3600 pixels are fitted and displayed. A high degree of uniformity and stability of the operation of the instrument emerges from all 3300 curves overlapping well with minor fluctuation while scanning over the area of interest. In addition, a more detailed analysis was carried out by fitting the in-phase (X) component of the magnetic resonance at each pixel and calculated the frequency fluctuation for the X (in-phase) $\Delta_X = 2.0 \%$.

An image is then generated following the procedure previously described. An image for the X component of the LIA is reported in Fig. 11 (b). The shape of the ring is captured with a visible crack. The crack size measured from Fig. 11 (b) is 14.4 ± 0.5 mm. Again, this is mostly due to the spreading of the field lines. The effect is here quite significant due to the increased lift-off corresponding to the introduction of the 1.50 mm rubber sheet.

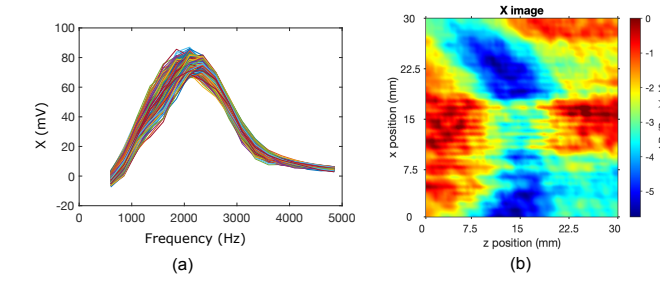


Fig. 11. Results for electromagnetic induction imaging at 2.0 kHz of the aluminium ring with a crack concealed behind a 1.50 mm thick rubber sheet. The frequency fluctuation for the X component is $\Delta_X=2.0$ %.(a) Plot of all 3600 pixels of the X (in-phase) of LIA used for imaging the rubber-shielded aluminium ring with the 0.68 mm crack. (b) The X image results. The scan area is 30×30 mm² image is built up with a pixel size of 0.5 \times 0.5 mm². The shape of the ring and the crack is clearly extracted from the background and the size of the crack is measured 14.4 \pm 0.5 mm.



Fig. 12. Photo of the taper gap between two aluminium plates placed close together. Each plate has a 100.0 mm length, 50.0 mm width and 20.0 mm thickness. A taper gap is generated from the left-hand side to the right-hand side with a maximum gap width of 1.57 mm. The structure is shielded by a 0.42 mm aluminium sheet with an additional 1.50 mm rubber sheet between the two block structure and the aluminium sheet.

C. A shielded taper gap

Two aluminium blocks, each measuring 100.0 mm in length, 50.0 mm in width and 20.0 mm in thickness, are positioned closely together, creating a gap whose size increases from the left-hand side to the right-hand side, as shown in Fig.12. On the right-hand side, the gap has a maximum width of 1.57 mm. The two blocks assembly is shielded by a 1.50 mm rubber sheet and a 0.42 mm aluminium sheet.

The shielded taper gap was imaged by translating the atomic magnetometer over it, covering an area of $60.0~\text{mm} \times 12.0~\text{mm}$ with a step size of 0.5~mm. All the steps of the procedure are as previously illustrated.

The magnetic resonances of four outputs of the LIA for

2880 pixels of imaging area are fitted and all curves overlap with each other with minor fluctuation in signal intensity. Later, the fluctuation of the frequency for X (in-phase) $\Delta_X = 2.4 \%$ is calculated by fitting the X (in-phase)

We then proceed with imaging the structure. All four images of the different outputs of the LIA display a V-shaped gap, as from Fig.13. This is mostly evident from the X component; a gradual change in the crack size is detected. The images also correctly show that two plates are almost in contact at around 1/3 of the length, starting from the left. In the X image, distance A represents the maximum taper gap, measured as 10.8 ± 0.5 mm whose actual size is 1.57 ± 0.01 mm; distance B is measured 5.8 ± 0.5 mm whose actual size is 0.84 ± 0.01 mm; distance C is measured 1.9 ± 0.5 mm and its actual size is 0.27 ± 0.01 mm. This is expected, as previously mentioned, due to the spreading of the field lines away from the target, an effect that becomes more pronounced for increasing lift-off. We notice that this makes the detection of small gaps and cracks easier.

IV. CONCLUSION

This work demonstrated a mechanically translatable EMI-AM imaging system that allows for sub-mm resolution and penetration through shields, an important requirement in the application area of non-destructive testing of the integrity of metallic structures. The sensor maintains high sensitivity while sweeping over a surface, in a magnetically unshielded environment. This was achieved by introducing several technical solutions which lead to enhanced performances, with respect to existing systems, and improved stability of the instrument while scanning over the target object.

We presented extensive evidence of the ability of our system to image through barriers, with the operating frequency appropriately lowered. This was done by imaging three different target samples presenting various types of gaps, and with different combinations of conductive and non-conductive barriers. We also demonstrated sub-millimetre resolution, validating the technique for the detection of sub-millimetre cracks in a metallic structure. Our results have direct impact on several Industry sectors, from rail transport and the construction sector to aerospace assembly, all applications where the ability to penetrate through the structure of interest or the barrier concealing it, is of paramount importance.

We notice that the present work introduced technical solutions for the management of environmental factors based on hardware developments. Further improvement in the instrument performances may be achieved by developing algorithms to reduce the detrimental effects of ambient noise on measurements, on the lines of ongoing work in the context of AM-enabled aeromagnetic measurement system on unmanned helicopters [23].

ACKNOWLEDGMENTS

This work has been funded by Innovate UK under project DELTA - Digitally Enhanced Low-cost Technology for Aerostructures (Project Reference: 10039976). With thanks for the programme management provided by Airbus industrial

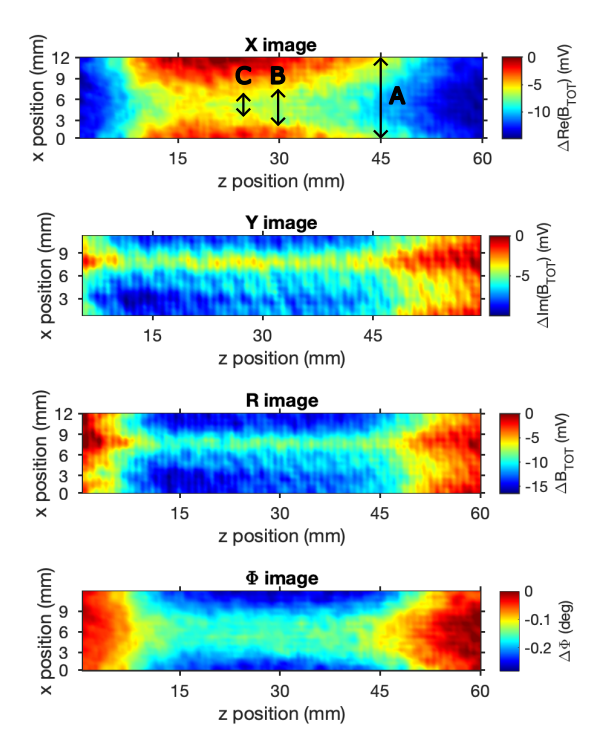


Fig. 13. Electromagnetic induction imaging of the gradual crack shielded by a 0.42 mm aluminium pad. The gap size widens from the left-hand side to the right-hand side, and its maximum is 1.57 mm. The operating frequency is 1.7 kHz. During the scanning, the resonance frequency fluctuation derived from fitting X component is found to be $\Delta_X = 2.4$ %. Eddy currents are generated by applying a 95mV signal, resulting in a current of 647.2 mA through the the RF inductor coil. Additionally, a 33.4 nT excitation field (B_{RF}) is applied. Scan conducted an area of $60.0 \times 12.0 \text{ mm}^2$ with a pixel size of $0.5 \times 12.0 \text{ mm}^2$ 0.5 mm². From the four components of images, a V-shape gradual crack can be observed, and the X image gives the best performance. Although the two blocks are put together tightly, they only closely touch each other at around 1/3 of the length starting from the left hand side, as shown in the image above. Distance A which corresponds to the maximum crack in the image was measured to be 10.8 \pm 0.5 mm while the actual size is 1.57 \pm 0.01 mm. Distance B in the EMI image is measured to be 5.8 ± 0.5 mm and in reality, it is 0.84 \pm 0.01 mm. Distance C was measured to be 1.9 \pm 0.5 mm and its actual size is 0.27 ± 0.01 mm.

contacts Tim Hall (tim.hall@airbus.com) and Amer Liaqat (amer.liaqat@airbus.com).

REFERENCES

- [1] H. Griffiths, "Magnetic induction tomography," Measurement Science and Technology, vol. 12, no. 8, p. 1126, 2001.
- [2] Y. He, G. Tian, H. Zhang, M. Alamin, A. Simm, and P. Jackson, "Steel corrosion characterization using pulsed eddy current systems," *IEEE Sensors Journal*, vol. 12, p. 2113, 2012.
- [3] H. Sun, T. Wang, D. Lin, Y. Wang, and X. Qing, "An eddy current-based structural health monitoring technique for tracking bolt cracking," Sensors, vol. 20, no. 23, 2020.
- [4] A. Vertiy, V. Uchanin, V. Pavlikov, S. Zhyla, O. Shmatko, and E. Tserne, "Eddy current tomography for visualization of cracks in aircraft riveted joints," *Radioelectronic and Computer Systems*, vol. 0, no. 3, pp. 94–113, 2021. [Online]. Available: http://nti.khai.edu/ojs/index.php/reks/article/view/reks.2021.3.08
- [5] J. Ge, F. Yu, T. Tomizawa, H. Song, and N. Yusa, "Inspection of pitting corrosions on weld overlay cladding using uniform and rotating eddy current testing," *IEEE TRANSACTIONS ON INSTRUMENTATION AND MEASUREMENT*, vol. 70, 2021.

- [6] U. C. Thibbotuwa, A. Cort's, A. M. Casado, and A. Irizar, "Resonant eddy current sensor design for corrosion detection of reinforcing steel," *Sensors*, vol. 24, no. 13, 2024. [Online]. Available: https://www.mdpi.com/1424-8220/24/13/4211
- [7] I. Savukov, S. Seltzer, and M. Romalis, "Detection of NMR signals with a radio-frequency atomic magnetometer," *Journal of Magnetic Resonance*, vol. 185, no. 2, pp. 214–220, 2007.
- [8] D. Budker and M. Romalis, "Optical magnetometry," *Nature Physics*, vol. 3, no. 4, pp. 227–234, 2007.
- [9] A. Wickenbrock, F. Tricot, and F. Renzoni, "Magnetic induction measurements using an all-optical 87rb atomic magnetometer," *Applied Physics Letters*, vol. 103, no. 24, p. 243503, 2013.
- [10] A. Wickenbrock, S. Jurgilas, A. Dow, L. Marmugi, and F. Renzoni, "Magnetic induction tomography using an all-optical 87rb atomic magnetometer," *Optics Letters*, vol. 39, no. 22, pp. 6367–6370, Nov 2014. [Online]. Available: http://opg.optica.org/ol/abstract.cfm?URI= ol-39-22-6367
- [11] C. Deans, L. Marmugi, and F. Renzoni, "Through-barrier electromagnetic imaging with an atomic magnetometer," *Optics Express*, vol. 25, no. 15, pp. 17911–17917, 2017.
- [12] C. Deans, L. Marmugi, S. Hussain, and F. Renzoni, "Electromagnetic induction imaging with a radio-frequency atomic magnetometer," *Applied Physics Letters*, vol. 108, no. 10, p. 103503, 2016.
- [13] N. L. A. Wickenbrock, J. Blanchard, and D. Budker, "Eddy current imaging with an atomic radio-frequency magnetometer," *Applied Physics Letters*, vol. 108, no. 18, p. 183507, 2016.
- [14] P. Bevington, R. Gartman, W. Chalupczak, C. Deans, L. Marmugi, and F. Renzoni, "Non-destructive structural imaging of steelwork with atomic magnetometers," *Applied Physics Letters*, vol. 113, no. 6, p. 063503, 2018.
- [15] K. Jensen, M. Zugenmaier, J. Arnbak, H. Stærkind, M. V. Balabas, and E. S. Polzik, "Detection of low-conductivity objects using eddy current measurements with an optical magnetometer," *Physical Review Research*, vol. 1, no. 3, p. 033087, 2019.
- [16] G. Bevilacqua, V. Biancalana, Y. Dancheva, A. Fregosi, G. Napoli, and A. Vigilante, "Electromagnetic induction imaging: Signal detection based on tuned-dressed optical magnetometry," *Optics Express*, vol. 29, no. 23, pp. 37 081–37 090, 2021.
- [17] F. Fang and Z. Wang, "Electromagnetic induction imaging with a serf atomic magnetometer," *Optics Laser Technology*, vol. 182, p. 112144, 2025.
- [18] C. Deans, Y. Cohen, H. Yao, B. Maddox, A. Vigilante, and F. Renzoni, "Electromagnetic induction imaging with a scanning radio frequency atomic magnetometer," *Applied Physics Letters*, vol. 119, no. 1, p. 014001, 2021.
- [19] B. Maddox, Y. Cohen, and F. Renzoni, "Through-skin pilot-hole detection and localization with a mechanically translatable atomic magnetometer," *Applied Physics Letter*, vol. 120, p. 014002, 2022.
- [20] L. Marmugi, C. Deans, and F. Renzoni, "Electromagnetic induction imaging with atomic magnetometers: Unlocking the low-conductivity regime," *Applied Physics Letters*, vol. 115, no. 8, p. 083503, 2019.
- [21] H. Yao, B. Maddox, and F. Renzoni, "High-sensitivity operation of an unshielded single cell radio-frequency atomic magnetometer," *Optics Express*, vol. 30, no. 23, pp. 42015–42025, Nov 2022. [Online]. Available: https://opg.optica.org/oe/abstract.cfm?URI=oe-30-23-42015
- [22] H. Yao, H. Zhang, D. Ma, J. Zhao, and M. Ding, "In situ determination of alkali metal density using phase-frequency analysis on atomic magnetometers," *Measurement Science and Technology*, vol. 29, p. 095005, 2018.
- [23] J. Li, J. Ge, G. Zhang, Y. Li, L. Wu, X. Wu, and S. Fan, "Noise suppression for an aeromagnetic measurement system on an unmanned helicopter," *Review of Scientific Instruments*, vol. 95, p. 075106, 2024.



Han Yao Han Yao received her B.E. degree in measurement and instrumentation from Beihang University, Beijing, China, in 2015. In 2024 she received her PhD in Physics from University College London (UCL), London (UK). After a post-doctoral position at UCL, in October 2024 she was appointed to an Associate Professor position at the School of Physics, Nanjing University of Science and Technology, Nanjing 210094, China.



Ningzhen Yin Ningzhen Yin is currently pursuing an Msci degree in Physics at University College London, London, United Kingdom. Her current research interests include electromagnetic induction imaging and radio frequency atomic magnetometers.



Raymond Lee Raymond Lee obtained his BSc from the University of Washington, Seattle, WA in 2021, and his MSc in Quantum Technologies from University College London, London, UK in 2023.



Gehang Liu Gehang Liu obtained his BSc from the The Chinese University of Hong Kong (Shenzhen, China) in 2020, and his MSc in Electronics & Electrical Engineering from the University of Glasgow (Glasgow, Scotland, UK) in 2024. Immediately after his MSc, Gehang started his PhD at Univrsity College London.



Ferruccio Renzoni Ferruccio Renzoni received the M.Sc. degree in physics from the University of Pisa, Pisa, Italy, in 1993, the Ph.D. degree from the Technische Universitaet Graz, Graz, Austria, in 1998, and the Habilitation a diriger des recherches from Ecole Normale Superieure, Paris, France. He then spent two years in Germany, at the Institut fuer Laserphysik (University of Hamburg), Hamburg, Germany, and three years in France, at the Laboratoire Kastler Brossel (Ecole Normale Superieure), Paris. In 2003, he joined University College London,

London, U.K., as a Lecturer, to be then promoted to a Reader and a Professor.